

Capabilities of a FBG sensor system to monitor the inelastic response of concrete sections in new tunnel linings subjected to earthquake loading

Nicola Tondini*¹, Oreste S. Bursi¹, Alessio Bonelli¹, Manuel Fassin¹

¹University of Trento, Department of Civil, Environmental and Mechanical Engineering

Published version at:

Tondini N.*, Bursi O.S., Bonelli A. and Fassin M. (2015) Capabilities of a FBG sensor system to monitor the inelastic response of concrete sections in new tunnel linings subjected to earthquake loading, *Computer-Aided Civil and Infrastructure Engineering*, 30(8): 636–653, doi: 10.1111/mice.12106

Abstract: *In a comprehensive experimental campaign we investigated the capabilities of Fibre Bragg Grating (FBG) sensors in monitoring the inelastic response of new circular concrete tunnel linings, subjected to seismic events. The FBG sensors measured the strains of steel reinforcement to be treated by a Decision Support System (DSS). First, a set of four point bending tests was performed on tunnel substructures, with the aim of characterizing the cross section under cyclic loading and of designing an FBG sensor package for use in a unique full-scale test on a structure, which represented a complete circular section of the tunnel lining. Several types of FBG packages, to be embedded in and applied externally to the tunnel section, were tested to find the best solution. For comparison purposes, some standard devices were also used. The results of the experimental campaign are presented in detail, highlighting the performance of FBG sensors in reliable inelastic strain measurement of ductile concrete sections in seismic zones. Finally, the use of these data by a Decision Support System (DSS) allowed for the estimate of current structural conditions and damage at the monitored sections.*

1 INTRODUCTION

1.1 Background and Motivation

Structural Health Monitoring (SHM) of complex infrastructures is of primary importance for developing cost-effective maintenance strategies (Huang et al., 2014) and can help to identify structural and durability problems before they become critical, endanger public safety, and impede traffic flow (Cruz and Salgado, 2009; Adewuyi and

Wu, 2011; Cusson et al, 2011). With a rational choice and location of sensors (Raich and Liszkai, 2012), durability monitoring can supply valuable data that can be used to calibrate service life physic-based models in order to understand both complex interaction mechanisms, as soil-structure interaction and actual in-service structural behaviour.

Due to progress in construction techniques and sensing technology, tunnels are increasingly used to offer efficient road transport in congested cities and hilly areas. Today, modern transport networks demand longer and wider tunnels, built in increasingly difficult ground conditions. Many rail, road and metro-line tunnels are under construction in densely populated seismic prone areas. These areas require high safety levels; but tunnels have shown sensitivity to seismic events, with significant damage in cases such as the 1999 Kocaeli earthquake in Turkey and the 1999 Chi-Chi Taiwan and 1995 Kobe Japan events (Hashash, 2001). In the case of rail and metro tunnels, even moderate track deformation can cause derailing. Moreover, it is difficult to assess the damage and the residual capacity of a tunnel after a major earthquake and aftershocks.

The effects of an earthquake on a tunnel depend on the direction of propagation of the seismic waves with respect to the tunnel axis. When parallel, usually there are no important effects except at critical locations such as faults and stiffness discontinuity zones, which need a specific shear design. Conversely, due to shear strains in soil, transverse waves cause ovalisation of the originally circular section, a dangerous event for structural integrity that has been studied by several authors (Wang, 1993; Penzien and Wu, 1998; Penzien, 2000; Hashash et al., 2005). Emphasis is placed on circular sections, as obtained by machine-

boring, often used in major infrastructure projects. Most theories (Newmark, 1968) follow the free-field deformation approach, determining soil distortion and neglecting the presence of the lining and of the cavity; one advantage is that closed-form solutions are available. Moreover, methods that take account of lining flexibility improve the reliability of the solution (Penzien and Wu, 1998). Clearly, more advanced numerical methods also exist, requiring precise soil and seismic characterization of the site as well as numerical simulation (Kirzhner and Rosenhouse, 2000).

Tunnel linings are usually built using reinforced concrete, which under significant ground movement can exhibit a nonlinear behaviour. Only by recording and analysing their structural response, we can obtain an accurate evaluation of lining performance and perform a reliable damage detection (Khelifa and Guessasma, 2013, Nigro et al., 2014). In other words, tunnels need both a reliable FE model and a robust monitoring system especially during a seismic event.

Thanks to their durability properties, optical fiber sensors are well suited for long term monitoring (Hampshire and Adeli, 2000). With the rapid development of Fibre Bragg Grating (FBG) sensing in recent years, FBG sensors have been successfully applied in various fields, including civil engineering, geo-technology, oil and gas, damage detection and structural monitoring (Glisic et al., 2011). FBG sensors amply fulfil the demands of structural health monitoring of an underground structure, thanks to three main characteristics: (i) they can provide high-resolution strain information at specified points of a structure, with a resolution of about 5 microstrain; (ii) they can be arranged in cascade to form a distributed system of sensors along a common fibre optical cable; (iii) the sensors can be interrogated simultaneously using a single source/detection unit. Other parts of the same structure can be independently monitored by dedicated fibre cables and FBG arrays, using the same optical spectrum. Additionally, FBG sensors offer high sensitivity, excellent reproducibility and reliable stability; but are also resistant to harsh environmental conditions, such as corrosion, humidity, electromagnetic fields etc.

The innovation today, is the use of distributed sensors for average strain, temperature and integrity monitoring (Zhang et al., 2006; Guemes et al., 2010). A distributed sensing system is, by its nature, well suited to and efficient for monitoring tunnels, which are structures with kilometre scale lengths. Depending on the tunnel cross-section and on the time of installation of the monitoring system (new structure: sensors can be embedded; existing structure: surface mounting only is possible), differing sensor network types can be adopted. In this respect, Glisic and Yao (2012) applied a distributed sensor system based on fibre optic sensors using Brillouin scattering to monitor a concrete pipeline subjected to earthquake-induced ground movement.

1.2 Scope

In view of these benefits, the MONICO project was funded with the aim of developing a Decision Support System (DSS) capable of estimating current structural conditions and damage at the monitored areas in tunnel cross-sections as well as the overall structural condition of new tunnels.

Monitoring of concrete structures by means of FBG fibres is widely employed (Rodrigues et al., 2010; Habel and Krebber, 2011; Wu and Adewuyi, 2011), measuring cracking, displacement, vibration control and other parameters. A common range for such reinforced concrete structures found in literature is $\pm 1000 - \pm 5000$ microstrain (Majumder et al., 2008; Kerrouche et al., 2009). The novelty hereinafter is the assessment of FBG sensor capabilities in monitoring the inelastic response of a tunnel lining, when subjected to seismic loads, in full-scale tests. Moderate to strong seismic events can entail high inelastic curvature demand on concrete members, the bending associated with yield of the reinforcement steel. In this study, the target strain range was set to ± 10000 microstrain (1%), to be measured by FBG sensors for ductile concrete sections.

2 THE MONICO EU PROJECT

MONICO is a project funded by the European Union within the 7th research programme framework. As mentioned above, the main objective of MONICO was to ensure the safety of seismic-vulnerable tunnel cross-sections or sections where very high standards of safety are required, by developing a DSS that relies on information provided by fibre optic sensors; the information then allowing real-time assessment of the structural reliability of the tunnel lining (Loupos et al., 2011).

The DSS was developed by incorporating two structural modules: the Expert System and the Data Base. The former acts as a controlling interface between the user and the system and coordinates the other modules. The user can estimate the actual structural condition at the monitored parts of the tunnel cross-sections as well as the overall structural condition of the cross-section.

Moreover, by means of the Data Base module the user can examine the trends of strain and structural condition of the monitored sections and of the entire tunnel lining, under the effects of past earthquakes. The DSS provides real-time warning of abnormal situations and allows the end-user to examine different scenarios for hypothetical situations. In detail, in order to ensure the safety of vulnerable tunnel cross-sections, fibre optic sensors providing a real-time remote deformation sensing capability, are integrated with software that collects and processes data and assesses the structural reliability of the lining. The fibre optic sensors record deformations in 8 locations of the tunnel cross-section, as depicted in Figure 1a, where the origin of θ -

coordinate and the direction of monitored deformations are also depicted. These deformations are then converted to strains, curvatures, deflections, stresses, bending moments and axial forces which are monitored so that they do not exceed limit values. Thus, local ductility of the monitored sections under operating loads is assessed deterministically and stochastically by varying the material properties represented by mean and standard deviation. Additionally, the history of deformations during an earthquake are processed in order to derive the local damage at specific monitored locations according to an energy-based damage index (Chai et al., 1995) based on the widely known damage model developed by Ang and Park (1985). In detail, it is expressed as follows

$$D = \frac{\chi_m}{\chi_{um}} + \frac{\beta^*(E_h - E_{hm})}{M_y \chi_{um}} \quad (1)$$

where:

χ_m is the maximum response curvature; χ_{um} defines the maximum curvature under a monotonic loading; M_y is the yield moment of the section; β^* represents a strength deterioration parameter characterizing the damage contribution owing to cumulative plastic strain energy; E_h and E_{hm} are the plastic strain energy per unit length dissipated by the section, e.g. $E_h = \int (Md\chi)$ during the earthquake -cyclic loading- and during a monotonic loading, respectively. Possibly, χ_{um} , E_{hm} , and M_y can be experimentally estimated.

The degree of damage was established according to the following conditions suggested by a project partner (Bairaktaris et al., 1998):

1) $D < D_1$ that corresponds to a condition where no plastic hinges form; $D_1 = E_{u1}/E_u$ where $E_{u1} = 0.75M_y\chi_y$ with M_y the bending moment at yielding of rebars and χ_y the corresponding curvature (see for clarity, Figure 13) and E_u is the available internal energy, equal to the area of the hysteretic envelope;

2) $D_1 \leq D \leq D_2$ that sets the formation of the first plastic hinge in a concrete section; $D_2 = E_{u2}/E_u$, where $E_{u2} = E_{u1} + 0.5(M_y + M_r)(\chi_r - \chi_y)$, M_r and χ_r are the maximum resisting

bending moment and the corresponding curvature, respectively;

3) $D_2 \leq D \leq 1$ that corresponds to failure of a concrete cross section.

The thresholds D_1 and D_2 were quantified in Subsection 5.2 for the Case Study to hand and are consistent with those suggested in the literature. For a survey, see William and Sexsmith (1995), among others, which reported typical values of 0.11 and 0.77 for D_1 and D_2 , respectively, for concrete columns.

Based on local damage indices after a seismic event, the global structural condition of the tunnel is stochastically estimated through the Monte Carlo Simulation (MCS) method (Hammersley and Handscomb, 1975), where the Latin Hypercube Sampling (LHS) method is selected in order to reduce the computing effort (Iman and Conover, 1980). In detail, a nonlinear Finite Element model of the tunnel is developed a priori with material and geometrical properties, i.e. the stress-strain and moment-curvature relationships that represent the stochastic variables. Then, a spectrum-compatible reference seismic input representative of the site is applied to the tunnel finite element (FE) model and a series of dynamic nonlinear analyses are performed by varying material and geometrical properties. In this way the extrapolation of the damage indices to other critical cross sections is possible as well as the estimate of the structural reliability of each section of the tunnel by means of a First Order Reliability Method (FORM) (Ditlevsen and Madsen, 1996), as illustrated in Figure 1b. The pursuit of an optimal fibre optic system is fundamental to provide reliable data on the basis of which the DSS works and a set of experimental tests with this aim was deemed necessary. Thus, in this respect, this paper presents the subset of the MONICO project that investigated experimentally the fibre sensor system performance in monitoring tunnel linings, by evaluating the inelastic response due to seismic loading. A comprehensive experimental campaign was carried out, based both on substructure tests and on a full-scale test. These tests also served to find the best fibre package and to characterize the seismic behaviour of the tunnel.

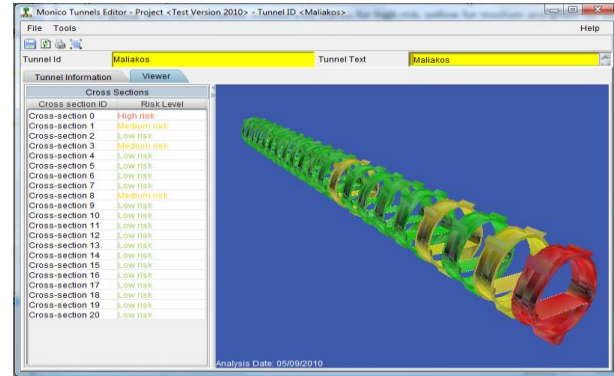
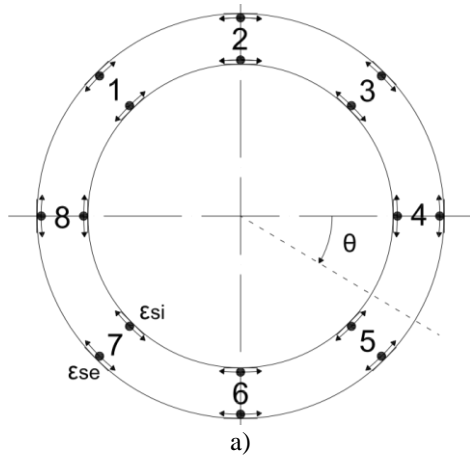


Figure 1 a) Locations of the monitored points in a tunnel cross section; b) tunnel in the developed DSS. Each cross-section coloured according to estimated reliability as an output of the global structural condition module

3 DESIGN OF TUNNEL LININGS AND TEST PROGRAMME

3.1 Seismic Design of a Metro Tunnel Lining

3.1.1 Tunnel features and soil characteristics. First, a benchmark tunnel lining with a circular pipe section was selected. The actual tunnel is in Rome, Italy. The outside diameter was 4.8 m, lining thickness 0.2 m and the tunnel axis was at 20 m below ground level. The elastic modulus and the Poisson coefficient of the lining concrete were taken as 31.4 GPa and 0.2 respectively. For soil characteristics, the elastic modulus and the Poisson coefficient were set to 84 MPa and 0.49, respectively, and the height of the water table above the lining was equal to 5 m. The density of the soil was 1800 kg/m³ and the overload was 2 kN/m². The seismic action considered at the Life Safe Limit State (LSLS) was equivalent to a design reference peak ground acceleration (PGA) on type A ground (rock) of 0.16 g, as expected in Rome with a nominal life of 100 years; an importance factor IV entailing a reference life of 200 years and a return period of 1898 years (Ministero delle Infrastrutture, 2008). This induced a PGA in a type D ground (deposits of loose-to-medium cohesionless soil, S=1.752) of 0.28g; a peak ground particle velocity of 0.319 m/s (Ministero delle Infrastrutture, 2008); and an effective shear wave propagation velocity of 125.1 m/s, determining a maximum soil shear strain of 0.26%; this value represented the input for cross section design. In the spirit of Performance-based Earthquake Engineering, we examined also the Collapse Prevention Limit State (CPLS), which is characterized by a 5% of probability of exceedance in the reference period, i.e. 200 years in this case. The return period and the PGA increased to 2475 years and 0.30g, respectively. The PGA values corresponding to LSLS and CPLS are typical of moderate/high seismic areas in Europe (ESD, http://www.isesd.hi.is/ESD_Local/frameset.htm).

3.1.2 Determination of stresses. Attention is limited here to ovalisation of circular tunnels, as estimated by equations proposed by Penzien and Wu (1998). These provide lining stresses due to: (i) the self-weight of the soil, (ii) the overload and (iii) seismic deformation under the basic assumption of deep tunnel and homogeneous soil. The effect of the lining stiffness are also taken into account. Moreover, in the Penzien relationships (Penzien and Wu, 1998) it is assumed that no soil deformation occurs as a consequence of the tunnel boring method; a condition of full slip was considered, between soil and tunnel. In general the aforementioned relationships describe the dilatational- and shear- type stresses due to the acting loads as a function of two coefficients α_d and α_s^{sn} , accounting for soil-lining interaction through relevant stiffnesses:

$$\alpha_d = \frac{E_l A_l (1 + \nu_s)}{R E_s (1 - \nu_l^2)}, \quad \alpha_s^{sn} = \frac{3 E_l I_l (1 + \nu_s) (5 - 6 \nu_s)}{R^3 E_s (1 - \nu_l^2)} \quad (2)$$

where the subscripts *s* and *l* denotes soil and lining, respectively; *A* denotes the unit length cross section, *E* the elastic modulus, *R* the radius and *ν* the Poisson's Ratio. The inward diameter change owing to radial (Δ_{d1}) and to shear-type stresses (Δ_{s1}) was evaluated as a function of the above reported coefficients and soil characteristic parameters for each loading condition. Once Δ_{d1} and Δ_{s1} were determined, thrust, bending moment and shear effect were evaluated. For instance, bending moments are characterized by the following relationship,

$$M_l(\theta) = \frac{3 E_l I_l \Delta_{s1}}{2 R^2 (1 - \nu_l^2)} \cos(2\theta). \quad (3)$$

With regard to the seismic action, its distribution exhibits a phase angle of 45° with respect to the seismic propagation direction.

Due to the circular shape and under static loading conditions, overall stresses are equivalent to an almost uniform compression load with limited bending and shear stresses. The overall stress state derives from the combination of the three basic loads described above and detailed here. For each condition, the contribution due to tension and shear stresses is computed; then, the internal forces are evaluated. The typical distribution of internal forces described by Equation (3) is a crossed sinusoid, see Figure 2, in agreement with Szechy (1970). The proposed estimate is reliable for typical tunnel depths. Moreover, the maximum and minimum force values are shown in Table 1.

As a result of the aforementioned loads, using both static and seismic LSLS combinations described above, it emerged that the tunnel cross-section was satisfactory, in terms of strength. Design checks for a 50 mm C25/30 concrete cover and 7+7 16 mm diameter B450 reinforcing bars, are shown in Figure 3a. In addition, Figure 3b illustrates the moment-curvature diagram of the section associated with the maximum and minimum thrust. As expected, compression stresses increase section strength but decrease ductility. Moreover, the moment-curvature diagram of the section, see for instance Figure 4a, helped estimate the curvature demand under seismic loading and check whether FBG sensors were actually capable of measuring strains beyond yield.

The bending moment distribution obtained using the Penzien and Wu method (1998) is characterized by a sinusoidal shape that exhibits a low gradient around the maximum and minimum moment, i.e. in the plastic hinge region -the length of which is estimated in Subsection 3.2-. Hence, this region can be treated as at constant moment, as shown in detail in Figure 2b. In particular, the reader can observe that the maximum moment amplitude ($\Delta M/M_{max}$) varies less than 15% over 1 meter along the circular tunnel

lining. Thus, pure bending tests on substructures can be realistic.

Table 1

Maximum and minimum characteristic values of internal actions based on Penzien's theory (Penzien and Wu, 1998)

	Load case:	Soil weight	Overload	Seismic action	Overall
Maximum actions	Bending moment [kNm/m]	35.08	0.03	49.28	84.38
	Thrust force [kN/m]	-676.67	-4.65	41.07	-640.25
	Shear action [kN/m]	28.79	0.02	40.44	69.25
Minimum actions	Bending moment [kNm/m]:	-35.08	-0.03	-49.28	-84.38
	Thrust force [kN/m]:	-735.13	-4.70	-41.07	-780.89
	Shear action [kN/m]:	-28.79	-0.02	-40.44	-69.25

3.2 Test Specimens

3.2.1 Substructure specimens. In the literature, see Williams and Sexsmith (1995), and Bursi and Ferrario (2003), it was found that a damage index for concrete members must be closely related to the plastic hinge length, for which estimates with common formulae show large dispersion. This problem was also related to the fibre length to be used in the full-scale experiment, in order to employ

the standard relationship $\chi = \frac{\Delta\phi}{\Delta s}$, where χ defines the

mean curvature, $\Delta\phi$ the plastic hinge rotation and Δs the corresponding length. To overcome these problems and to characterize the moment capacity and the plastic rotation of concrete sections, a series of tests on substructures was planned; and these tests also helped to select adequate packaging for FBG sensors. As described in Subsection 4.2, these simple tests were performed to gain information on: i) optimal configuration, ii) location and iii) length of fibres to be installed in the full-scale tunnel specimen. Therefore, the substructure specimens were characterized by the same dimensions, materials and prestressing foreseen in the full-scale test.

As discussed in Subsection 3.1, the maximum bending moment over one meter of tunnel lining was almost constant. Therefore, four point bending tests on substructures were used to reproduce the fairly uniform bending stress exhibited at areas of maximum values.

The cross-section specimen and the load scheme are shown in Figure 4. Each specimen had cross-section 1000 mm x 200 mm and length 3000 mm. These were of C25/30 concrete and the rebars were 7+7 Φ 16 B450C steel.

The relevant hinge length l_{pl} was calculated from two different relationships:

(1) Nilson and Winter, (1986)

$$l_{pl} = 0.5d + 0.05z = 16.5 \text{ cm} \quad (4)$$

where d is the effective depth of the cross-section and z is the distance from the critical section of the plastic hinge to the point of contraflexure.

(2) OPCM 3274 (2003)

$$l_{pl} = 0.1L_v + 0.17h + 0.24 \frac{d_{bl} f_y}{\sqrt{f_c}} = 48 \text{ cm} \quad (5)$$

where L_v is the shear span; h defines the height of the section; d_{bl} is the average diameter of longitudinal rebars; f_y defines the yield strength of the reinforcement steel and, f_c is the concrete compression strength. The bending moment between load points was imposed by increasing the vertical displacement through an actuator, whilst the prestressing force, equal to 600 kN, was applied by means of a pair of prestress dywidag rods. Since the plastic hinge length was estimated at between 16.5 cm and 48 cm, see equations 4 and 5, the selected span for uniform bending moment was 40 cm, between the two load points. This type of test provided the flexural ductility and the strength characteristics without considering any shear effect.

3.2.2 Full-scale specimen. The tunnel lining test specimen was extracted from the metro tunnel presented in Subsection 3.1. In detail, a circular section with outside diameter of 4.8 m, thickness 0.2 m and width 1 m was chosen. As for seismic conditions, although the seismic wave propagation direction is mainly vertical, it can be inclined for shallow tunnels or if the site is near a fault. The worst case for the structural safety of a lining occurs when seismic waves propagate at an angle of 45°, because seismic action maxima, in this case, sum up with the static load maxima. Hence the maximum moment was reached at 0°, 90°, 180° and 270°. This was the choice for the lining test set-up shown in Figure 5, where two electro-hydraulic actuators were located orthogonally to one another.

The axial force was applied by steel ties carried by a system of cylindrical bearings; this proved to be the most efficient solution as to friction losses. The same load in substructure tests, 600 kN, was applied to the full-scale specimen using three 24 mm high-tensile steel cables, which were prestressed with two hollow jacks of capacity 1000 kN each. The cable tension was transferred to the ring by vertical steel rollers, visible in Figure 5. The ovalisation of the section caused by the two hydraulic actuators offered good representation of the stress state predicted by the simplified Penzien method (Penzien, 1998; Hashash et al., 2001; Hashash et al., 2005).

3.3 Test programme and load protocols

The experimental campaign was split into three parts:

- Tests on materials.
- Tests on substructures.
- Test on a full-scale specimen of a tunnel lining.

Tests on materials were carried out to characterize their mechanical properties. Table 2 reports the procedure used for each test of type b) and c).

3.3.1 Test typology applied to substructures. Monotonic and cyclic tests were performed. The monotonic test was performed with displacement control to acquire both its force-displacement response and maximum ductility. The results of the monotonic test served to calibrate the subsequent cyclic tests.

In cyclic tests, the ECCS procedure (Technical Committee 1, TWG 1.3, 1986) was applied. These provisions, mainly conceived for steel structures, were thought suitable for this type of test in the absence of a specific cyclic test procedure for concrete structures. The load protocol was designed on the basis of a conventional

displacement δ_y , which represented the elastic-plastic transition of the cross section behaviour. The cyclic loading hence consisted of a series of cycles in displacement control which were increased proportionally to the δ_y value, as shown in Figure 6. In detail, the monotonic test on substructures provided deflection at yield equal to 19 mm. In the cyclic test, it was decided to set a maximum displacement to $4\delta_y = 76$ mm; in fact in the monotonic test, it was observed that the beam was destroyed at a displacement of about 60 mm, entailing high loss of stiffness and strength. Finally, loads were applied in two phases in both monotonic and cyclic tests: i) initial axial specimen prestress with dywidag rods; and ii) vertical displacement by means of a hydraulic actuator.

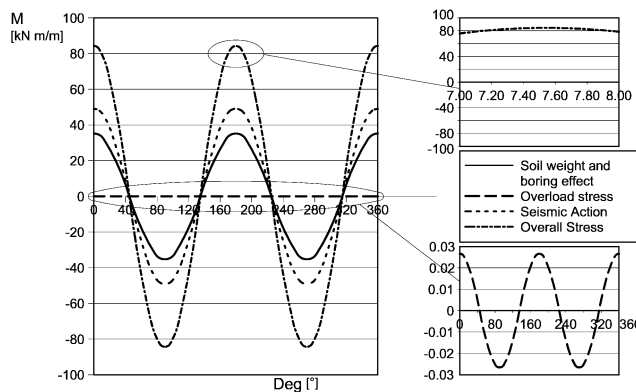
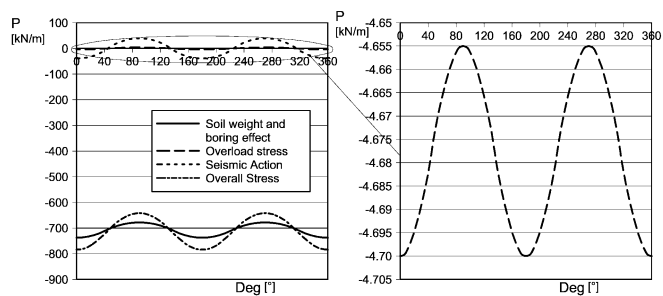


Figure 2 a) Thrust action estimated by means of the Penzien and Wu (1998) formulae; b) bending moment estimated by means of Penzien and Wu (1998) relationships

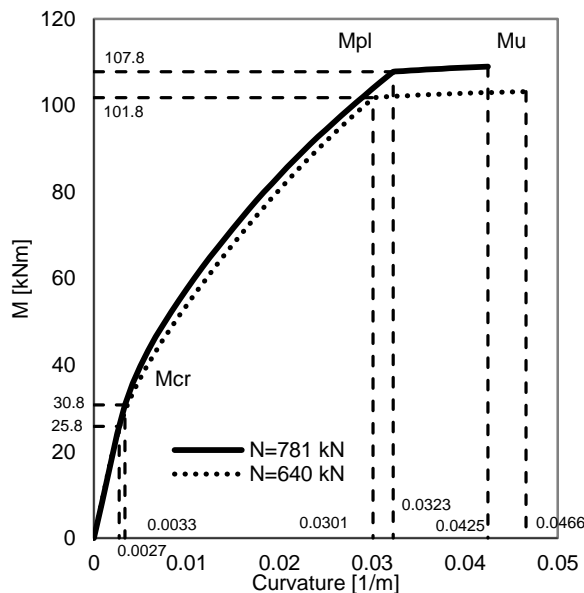
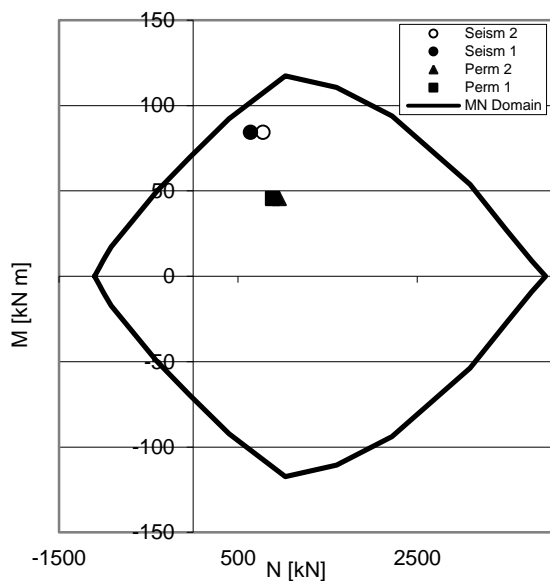


Figure 3 Transversal section of the specimen: a) M-N diagram relevant to Static and Seismic LSLS actions; and b) Moment – Curvature diagram relevant to maximum and minimum thrust action estimated by Penzien and Wu (1998) relationships

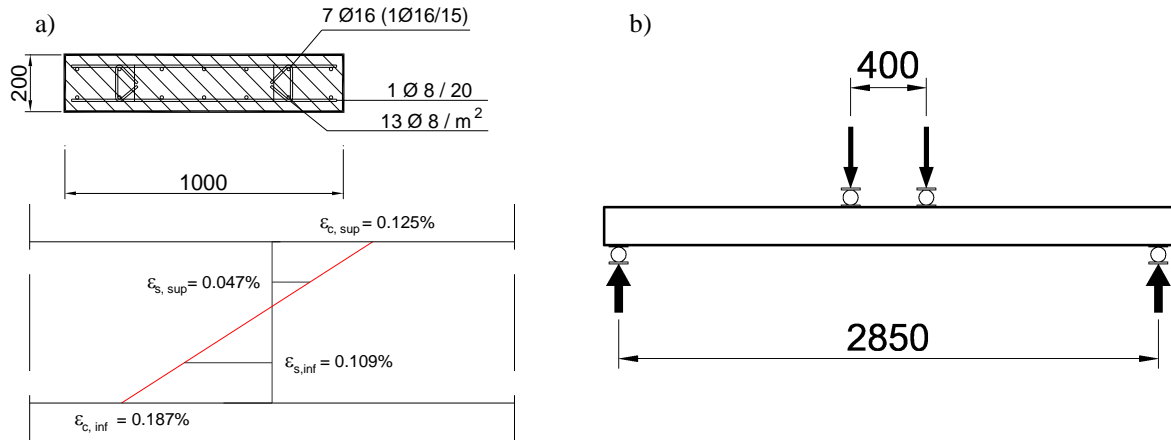


Figure 4 Test set-up for the SSC2 cyclic test on substructure: (a) cross section specimen and relevant experimental strain distribution owing to the design earthquake defined in Subsection 3.1; (b) four point loading scheme (dimensions in mm)

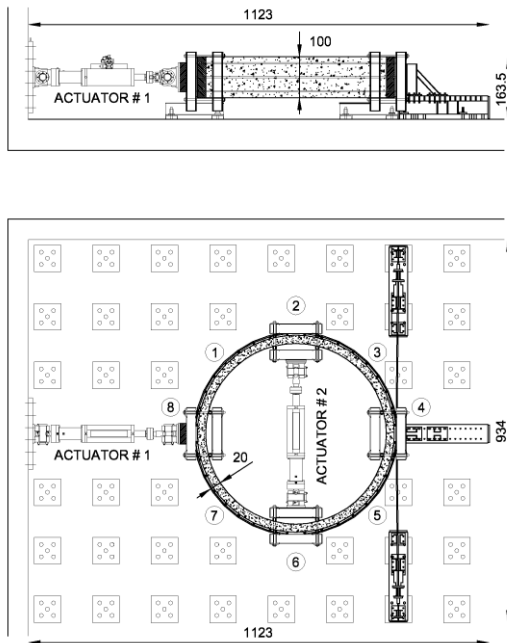


Figure 5 Tunnel lining: plan, lateral view (dimensions in cm) and actual full-scale specimen

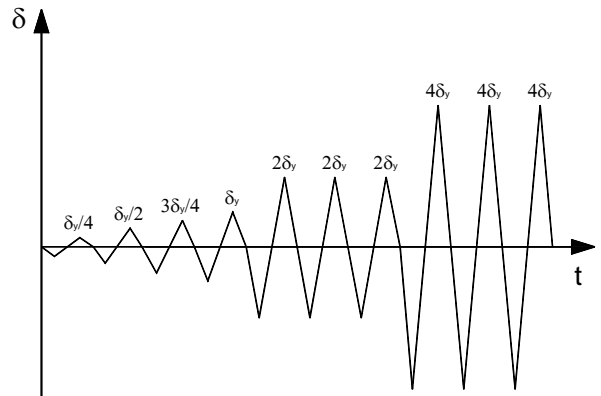


Figure 6 Loading protocol according to the ECCS (1986) procedure

3.3.2 Test typology applied to the full-scale specimen. Because one full-scale specimen was available, only one cyclic test was performed, by means of the ECCS procedure. Thus, the estimate of the ring yield displacement $\delta_{y,ring} = 60$ mm to be used with the ECCS (1986) loading protocol, was based on both the result of the monotonic test SSM1 of Table 2 and an FE model of the whole ring.

4 FIBRES AND THEIR PACKAGING

With regard to fibre sensors, the DSS was conceived for use with two different types of optical fibres, namely: i) Fibre Bragg Grating sensors; and ii) Brillouin fibre optical sensor technology. However, this paper focuses only on FBG sensors and on their ability to capture the inelastic behaviour of tunnel lining subjected to moderate/high seismic loading.

Three FBG configurations were employed: FBG sensors attached to reinforcement bars, either i) bonded to or ii) unbonded in concrete; and iii) FBG sensors externally mounted on metal holders welded to reinforcement bars

through access holes left during casting. Sensors embedded in concrete were protected by the glue used to attach them in the groove on rebar pieces; whilst acrylate coating and a 900µm tubing were used for external fibres. Acrylate coating poses issues at higher strain levels when embedded in or bonded to a material such as concrete, indeed (Her and Huang, 2011). However this was not our case, because acrylate coating was only used for external fibres; thus, no interaction between fibre and concrete occurred.

Since the aim was to assess the capabilities of fibre optic sensors in predicting the nonlinear behaviour of instrumented sections with structural steel, a value of strain of at least 1% was set as a target. In fact and on the basis of the experimental moment-curvature diagram reported in Figure 13, the seismic demand on the tunnel implied a maximum rebar deformation $\epsilon_{s,inf} = 0.109\%$ as illustrated in Figure 4a. Considering the ability of the system to monitor section damage evolution associated with the developing of a plastic hinge and a minimum strain ductility of 10, $\pm 1\%$ strain demand was deemed appropriate. The fibre interrogation unit used had spectral limits between 1515 nm and 1590 nm, respectively, i.e. a spectral range of 75 nm. For measuring a 1% deformation, i.e. a high strain demand, a higher wavelength spacing that reduced the number of fibre sensors per gauge was needed. In fact, in terms of wavelength shift, a maximum strain of 10000 microstrain (1% deformation) implies 12 nm strain (3nm is 0.25% deformation), assuming a typical FBG strain sensitivity of 1.2 pm/µε (Rao, 1997). This value can entail a positive or a negative shift, for tensile or compression strain, respectively. Since the expected strain for the embedded sensors was either compressive or tensile, a double spacing of wavelength between the sensors, i.e. 24 nm of bandwidth per sensor was allocated. Given the total wavelength range owing to the operational range of the interrogation unit, the number of sensors in an FBG array was limited to three; thus, the ability to sense 1% deformation, both in compression and in tension, was preserved. The wavelength allocation of three strain sensors on the same line is shown in Figure 7. The wavelength spacing of the temperature sensors was much smaller, around $\pm 1\text{nm}$ and $\pm 2\text{nm}$; it was enough for measuring temperature changes of over $\pm 1000\text{C}$.

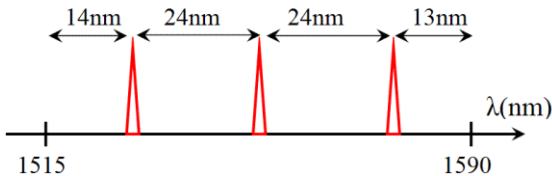


Figure 7 Spectral distribution of strain FBG sensors in the 75nm wavelength window. The sensor wavelengths were $\lambda_1=1529$ nm, $\lambda_2=1553$ nm and $\lambda_3=1577$ nm

Because in a reinforced concrete element major cracks form at a spacing of several centimetres, the unbonded sensor solution was conceived. As depicted in Figure 8, rebars undergo plastic deformation only at cracks, whereas between two cracks they remain in the linear range. Thus, if the base length of the gauge measurement is very short, as it is for FBG fibres, the probability that a sensor spans a crack is very small; consequently, the short-gauge sensor would measure the elastic strain of the rebar steel even though the concrete has cracked. In the unbonded solution, the strain measurement is obtained as an average over a long measurement base; thus, the long-gauge sensor is not influenced by local material discontinuities and inclusions. In sum, the related measurement provides information related to global rather than to a local structural behaviour.

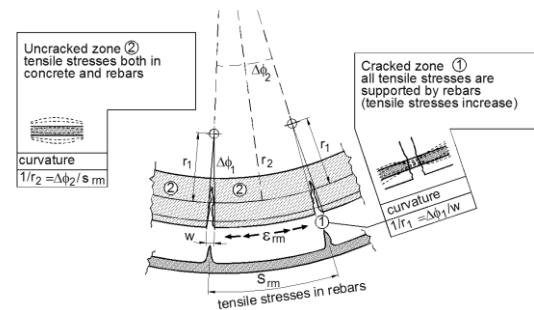


Figure 8 Deformed configuration of a reinforced concrete element subjected to bending

For the reinforced concrete section under study, the expected average spacing of cracks $s_{r,avg}$ was about 11 cm whereas the expected maximum spacing $s_{r,max} = 18$ cm (EC2-1 CEN, 2005). Thus, unbonded embedded fibre sensors spanning 40 cm, see Subsection 3.2.1, were "decoupled" from cracked concrete for a distance larger than $s_{r,max}$.

The external FBG sensors were mounted by welding two steel plates to the rebar cage and again at a distance larger than $s_{r,max}$. The installation of external FBG fibres was thought convenient when building the tunnel: the installation can be easily done after completion of the tunnel and replacement would be straightforward in the case of a fault. For the unbonded sensor solution, fibre prestrain was needed and the value ranged from 0.76 to 0.88%.

In addition to fibres and to check the reliability and accuracy of FBG sensors, we also used some traditional sensors such as potentiometer, LVDT and strain gauge displacement transducers, inclinometers and strain gauges. The instrumentation set-up was also improved on the basis of the results of previous tests.

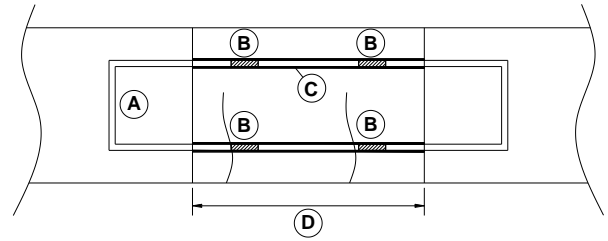
4.1 Fibre packages in substructure tests

To estimate their relative performance and to select the best strategy for the final full-scale test, the substructure

specimens were tested with the previously described FBG sensor configurations: either installed internal or external, either bonded to or unbonded in the concrete as shown in Table 2. Internal fibres were precast in the concrete. The package was fitted to longitudinal rebars in the zone where a plastic hinge was expected. In the SSC2 test the sensors were attached in the specimen by two smart stirrups, shown in Figure 9; they were made of two 10 x 10 mm steel bars with a 3 mm groove which contained fibres. In detail, the fibres were fixed in the groove with a shore D 96 epoxy resin. Then, the groove was filled with silicone to protect fibres. As described in Subsection 5.1, this method for internal FBG sensors based on a stirrup was not optimal. Hence, another solution was developed: the fibres were glued on ribbed bars with adequate anchorage lengths, of the same steel used in the specimens. An example of external FBG sensors after casting the substructure specimens is shown in Figure 12.

The internal fibre sensors were installed in two ways:

1. bonded to concrete: sensors were fastened to the steel, this being fully bonded to the concrete;
2. unbonded in the concrete: bonding between sensors and rebars was prevented by means of glue/tubing.



- A - Stirrup where FBGs are attached on
- B - FBGs
- C - Material to prevent bond
- D - Plastic hinge length

Figure 9 Stirrup equipped with FBG sensors embedded in the SSC2 specimen

Table 2 Fibres combinations used in different tests

<i>Test</i>	<i>Testing Procedure</i>	<i>Test acronym</i>	<i>Notes about fibres</i>	
Substructure Tests	1	Monotonic	SSM1	No fibre
	2	Cyclic ECCS	SSC1	No fibre
	3	Cyclic ECCS	SSC2	Internal bonded and unbonded FBG fibres
	4	Cyclic ECCS	SSC3	External unbonded FBG fibres
	5	Cyclic ECCS	SSC4	Internal and external unbonded FBG fibres
	6	Cyclic ECCS	SSC5	External unbonded Brillouin fibres
Test on Tunnel Lining	Cyclic ECCS	TLC1	FBGs with various configurations	

4.2 Fibre Packages in the Full-Scale Test

Based on substructure tests, the optimal fibre packages were employed extensively in the full-scale test. In particular, it was found that the unbonded solutions, both internal and external, see details in Figure 10 and Figure 11, respectively, provided a better estimate of rebar strains. Nevertheless, to get a complete picture of all package capabilities, a section of the tunnel ring was also instrumented with bonded fibres, i.e. Section #2 of Figure 15.

The distribution of the discrete FBG sensors was chosen based on the requirement for maximum strain at 8 points both of the inner and of the outer section of the tunnel lining. They were positioned symmetrically as shown in Figure 14. The total number of FBG sensors was based on the interrogation unit capabilities. Further sensors were added in two sections where plastic hinges were expected, i.e. in correspondence with the inner actuator. Further, temperature sensors were used to compensate for temperature-induced wavelength shifts of all fibre sensors. Hence, the FBG sensor system finally consisted of a total number of 40 sensors, as summarized in Table 3.

When acquiring data from fibres the target resolution was selected as high as 1 microstrain and a maximum sampling

rate of about 50 samples/sec was ideal for reproducing even the most rapid expected oscillations of a civil structure during an earthquake. The specimen was also instrumented with 16+4 standard displacement transducers and 6 load cells.

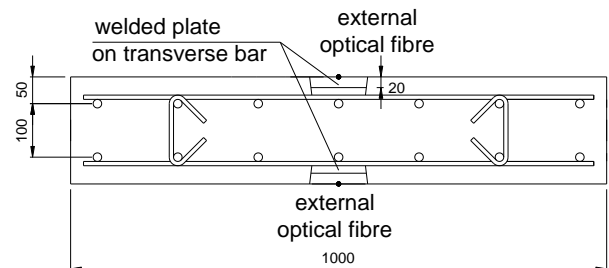


Figure 10 SSC3 specimen: transversal section with external unbonded fibre sensors

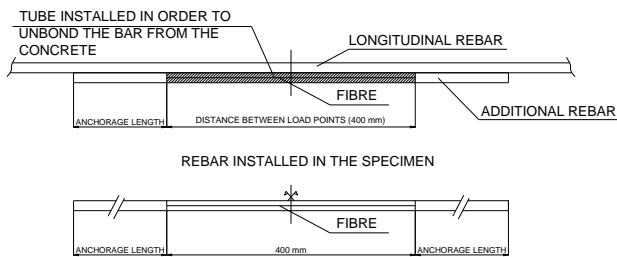


Figure 11 Plan view of internal unbonded fibre sensors installed in the SSC4 and TLC1 specimens

5 TEST RESULTS

5.1 Test Results on Substructures

In agreement with Table 2 and in order to experimentally evaluate the moment-curvature relationship of the tested section of Figure 4a, prior execution of the cyclic test series, a monotonic test was performed. The corresponding response of SSM1 specimen is shown in Figure 13, together with a trilinear approximation of the section capacity and the relevant seismic demand. With regard to cyclic tests, substructure responses are summarized herein. All substructure tests were instrumented with conventional sensors according to the set-up sketched in Figure 19.



Figure 12 External fibre sensors installed in the SSC3 specimen

In particular, the SSC2 test was selected to show the behaviour of internal bonded and unbonded fibres, whereas the SSC4 provided insight on the performance of the external package solution. Moment-rotation and moment-curvature curves relevant to the SSC2 specimen are shown in Figure 16. In detail, referring to Figure 19, plastic hinge rotation was derived from inclinometers ($\theta = inc2 - inc0$), whereas curvature was computed assuming plane sections, i.e. $1/r = (|\epsilon_{sup}| + |\epsilon_{inf}|) / h_{vs}$, by means of displacement transducers that measured displacements over the estimated plastic hinge length at the superior and at the inferior longitudinal rebar level, respectively. In detail, both for the top and the bottom measurements, two displacement transducers on a basis of 120 mm were located near in the

specimen middle-span and strains were estimated by considering the average deformation of the plastic hinge zone, i.e. $\epsilon_{sup} = (A3 + A1) / 240$, $\epsilon_{inf} = (A4 + A2) / 240$; h_{vs} was equal to 100mm.

There is some asymmetry, due to material imperfection; moreover, favourable hysteretic behaviour due to large energy dissipation is evident. Thus, this cross section appeared suitable for seismic applications. The responses of the bonded and unbonded fibre sensors during the SSC2 test for the lower beam face are shown in Figure 17.

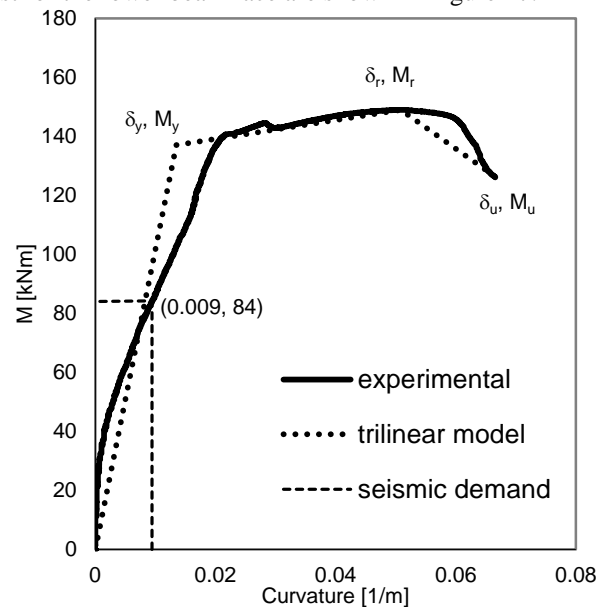


Figure 13 Experimental moment-curvature response of SSM1 specimen, piecewise approximation and seismic demand

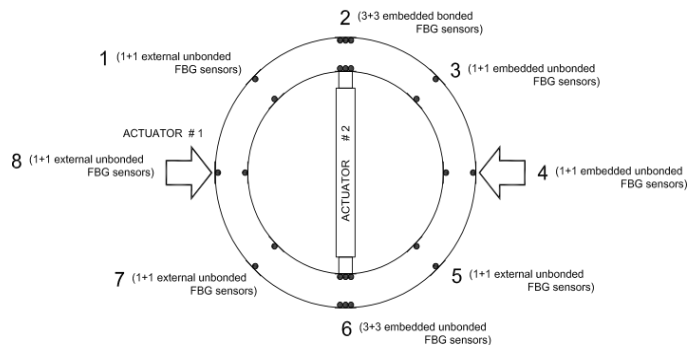


Figure 14 Distribution of fibre sensors along the inner and outer tunnel lining

We can note that even though the test was characterized by cycles with increasing displacement amplitude, the strain magnitude measured by fibre sensors reduced after the first cycle at $2\delta_y$. This behaviour, registered in both bonded and unbonded sensors was probably caused by detachment of the stirrups from the concrete owing to cracking. Moreover, the deformation in compression (-) was always less than that in tension (+), as cracks opened under tension. By

assuming plane sections and a perfect bond between concrete and rebars the strain state of the cross-section was estimated up to the $2\delta_y$ cycle, relying on data provided by: (i) strain gauge displacement transducers; (ii) strain gauges; and (iii) bonded FBGs. The relevant graph is shown in Figure 18, and we can see: (i) plastic behaviour from displacement transducer readings, (ii) plastic behaviour from strain gauge readings and (iii) elastic behaviour from fibre readings. At an amplitude of $2\delta_y$ the rebars had to be in the plastic range, as predicted by both displacement transducers and strain gauges. Strain values revealed by displacement transducers and by strain gauges were obtained as an average on a measurement base length of 120 mm, whilst the fibre sensors measured strains on a much shorter base length, i.e. about 5 mm. These differences were the caused discrepancies between measurements. As explained in Subsection 4.1, cracking was highly probable over the length of 11 cm – as confirmed in the tests – with a consequent strain increase; whereas over the 5 mm length concrete cracking was unlikely; so much smaller strains were detected.

	number of sensors
FBG	24

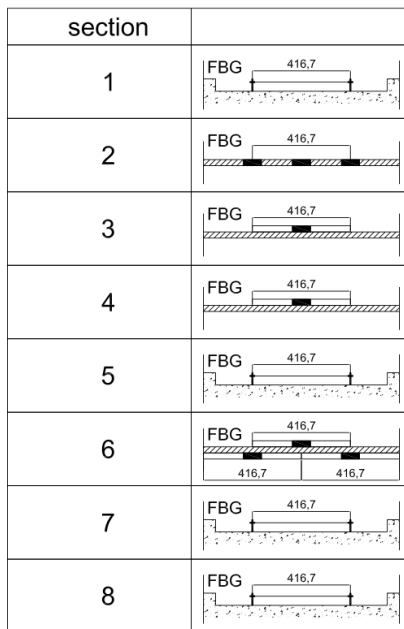


Figure 15 TLC1 Test: details of fibre sensors used at different sections of the tunnel lining. Dimensions in mm

Table 3

TLC1 Test: Strain and Temperature Fibre Sensors

12 gauges	1 strain + 1 temp. sensor (Sect. #1,3-5,7-8)	
4 gauges	3 strain + 1 temp. sensor (Sect. #2,6)	
Total	24 strain sensors	16 temp. sensors

Figure 20 shows the performance of the external fibre package compared to the internal one, which was a ribbed bar of the same material as the rebars. Data were obtained from the SSC4 test and both sensors were of the unbonded type. Both solutions could measure beyond 1% strain and so they were suitable for the target strain.

In sum, from the tests carried out on the substructures, we can state that:

- the substructures exhibited ductile behaviour characterized by large deformations in the plastic range associated with high energy dissipation, and hence, the cross-section used appears suitable for seismic loads;
- though both unbonded and bonded internal package solutions for fibres should allow for 1% strain measurement, fibre optic sensors, when mounted on a steel stirrup as for SSC2 specimen, were not capable of reliably measuring strains beyond a $2\delta_y$ displacement amplitude, which corresponded to about 0.2% strain. In fact, partial detachment of fibres from the steel stirrup or detachment of steel from concrete were the main causes. This behaviour led to the new package solutions employed in the other substructure tests and in the tunnel lining test: i) external installation of fibres on steel supports; ii) gluing fibres to ribbed bars of the same steel used in the specimens;
- the SSC4 test performance clearly highlighted the ability of both external and internal unbonded (with a portion of ribbed bar) package solutions to measure higher strains than the target value of 1%, established at the beginning of Section 4.
- short length strain measurements prevented an effective measurement of mechanical cross-section behaviour. In fact, the strain field was underestimated owing to measuring at positions without cracks. In this respect, external and unbonded fibres with 3 sensors in a row provided more accurate average values.

Finally, both monotonic and cyclic tests allowed both the experimental evaluation of the degradation parameter β^* involved in Equation (1) and of relevant damage index thresholds D_1 and D_2 , without the need of literature data. In detail, Figure 21 shows the damage limit domain, with $D=1$, for the section of Figure 4a. It was characterized by β^* of about 0.02, $E_{u1}=1.14$ KJ/m, $E_{u2}= 6.83$ KJ/m and $E_u=8.38$ KJ/m corresponding to $D_1=0.14$ and $D_2=0.85$, respectively.

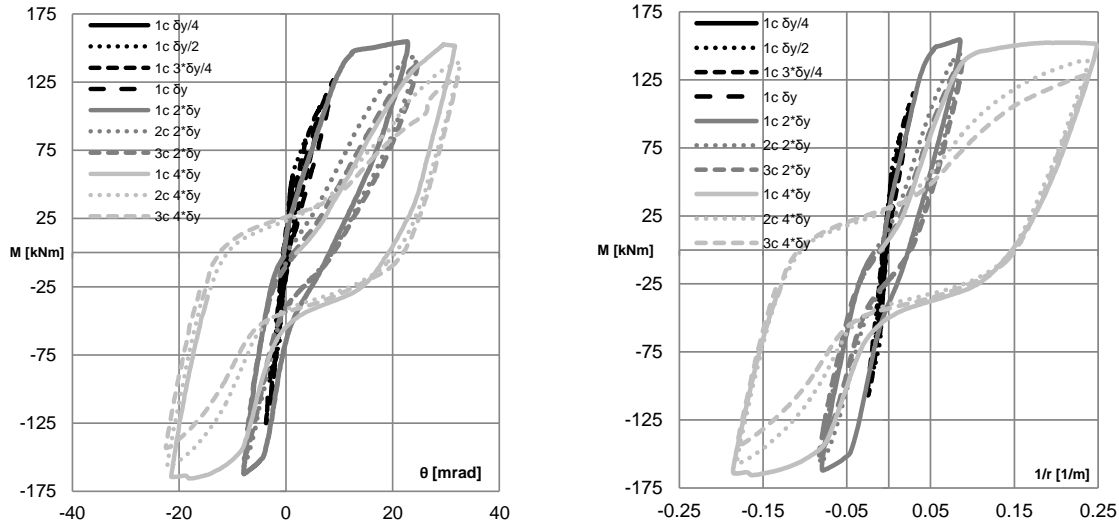


Figure 16 SSC2 test: a) moment –rotation curve detected with inclinometers; and b) moment-curvature relationship obtained from strain gauge displacement transducers assuming plane sections

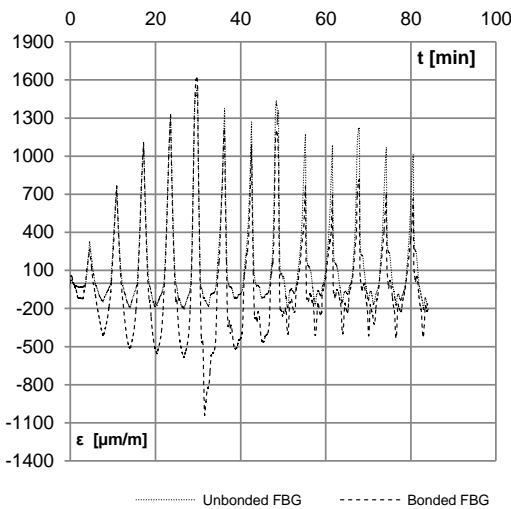


Figure 17 SSC2 test: strain values provided by bonded and unbonded fibre optic sensors located on the bottom side of the beam section.

5.2 Full-scale Tunnel Ring Test Results

During the full-scale test both conventional sensors and fibres were used. Referring to fibre results, both configurations reported in Figure 14 and Figure 15 were exploited. In detail, external fibres were installed with the configuration used for substructure tests; conversely in order not to modify the global behaviour of the reinforced concrete section, embedded fibres were installed on ribbed bars - with a small diameter of 8 mm- made of the same steel B450C used in the specimens. The quality of results was again corroborated by comparison with standard transducers.

To simulate the effect of soil and strains relative to prestressing, the full-scale specimen was prestressed by

tendons as shown in Figure 22a for Section #2. Average strain values at each section are presented in Table 4.

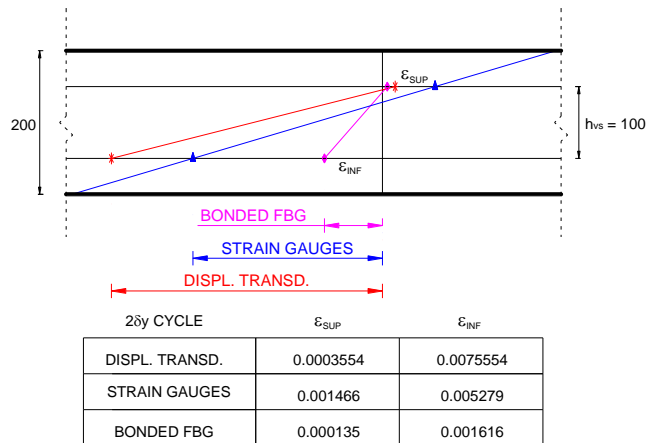


Figure 18 SSC2 test: strains at the longitudinal rebar level for the 2δ_y cycle with bonded fibres (dimensions in mm).

From Figure 22b and Figure 23, we can observe that embedded FBG fibres acquired data that were less disturbed than data from external FBG fibres located in sections without plastic hinges, i.e. Sections #1-3-5 and #7. The failure boundary in these figures represents the time at which the first section of the tunnel failed, i.e. Section #8. Temperature data, provided by the FBG fibres N. 2i, 2o, 3i, 3o, 4i, 4o, 6i and 6o, indicated temperature variations between 19.05 °C and 21.51 °C. The variation of about 2 °C in a 4 hour test was consistent with conditions.

Maximum deformation values for each instrumented section can be found in Table 5. As expected, fibres measured greater deformation in Sections #2, 4, 6 and #8, where plastic hinges formed. In detail, external FBG fibres

approached a maximum value of about 0.6% in Section #8, whilst internal FBG fibres reached a maximum value of 1.2% at Section #2.

All tunnel ring test data allowed for the application of the DSS summarized in Section 2; nonetheless, given the fact that only one test was conducted, mechanical parameters were considered deterministic. Assuming plane sections, the FBG strain evolution measurement in each cycle of the ECCS test protocol of Figure 6 allowed to quantify curvature values, and hence, to estimate bending moments acting on each section by means of standard constitutive models for concrete and structural steel. This calculation is depicted in Figure 24, where the damage evolution of each section is shown together with thresholds D_1 and D_2 . The damage value associated with Section #8 was the first to reach the D_2 value corresponding to failure. This prediction confirmed the actual failure highlighted in both Figures 22 and 23.

6 CONCLUSIONS

This paper investigated the capabilities of Fibre Bragg Grating (FBG) sensors for monitoring the inelastic response of a new circular tunnel lining subjected to seismic loading. It was located in a moderate to high seismic area in Europe, and to estimate the FBG capabilities, an experimental campaign based on substructure and full-scale tests was carried out. Several fibre package solutions were tested, such as bonded and unbonded in concrete; internal (embedded) and external sensors. The pursuit of an optimal fibre optic system was fundamental to provide reliable data to the DSS which, on the basis of experimental data, was capable of estimating current damage conditions by means of nonlinear FE analyses of a tunnel lining.

Firstly, the unbonded solution for fibre sensors classified as long-gauge sensors, both embedded and external, performed reliably at deformations in the inelastic range at strains higher than 1%; this value was estimated to be adequate for deformation demands of ductile concrete sections in moderate/high seismic areas. Such strains occurred both in the substructure tests and in the full-scale test.

Secondly, comparing the demand moment-curvature diagram with experimental results obtained by fibre measurements, nonlinearities were detected. Thus, a circumferential unbonded fibre package with 3 sensors in a row, over the maximum expected spacing of cracks and within the expected plastic hinge length, was suited to structure monitoring, where high nonlinear behaviour owing to seismic loading was expected. In fact, in the full-scale test, the system clearly measured higher strain values at sections of the tunnel where plastic hinges formed. The external FBG sensors approached a maximum strain value of about 1.2%. Further, embedded fibres acquired readings that were less disturbed than those provided by external fibres located at sections without plastic hinges. Due to simple application during both the construction process and also for replacement during the service life of the structure, an external solution for the fibre package may be preferable. Moreover, the results obtained by FBG sensors correlated well with those of standard transducers. Lastly, the use of these data by a DSS allowed for the estimation of current structural conditions and damage at the monitored sections.

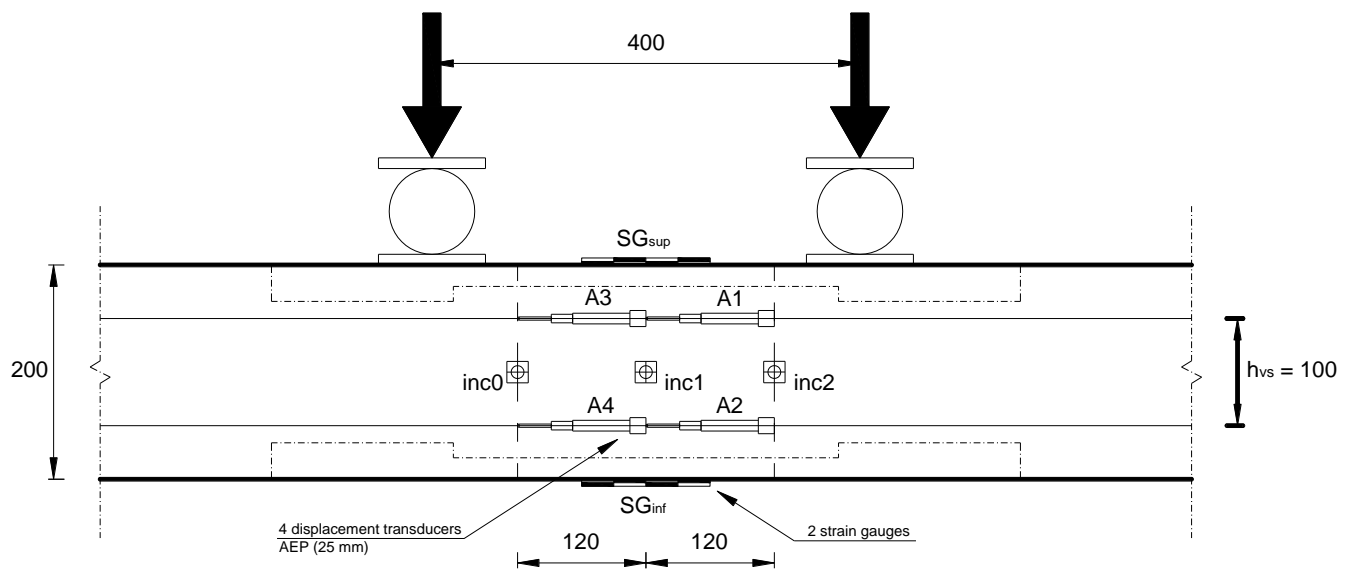


Figure 19 Strain gauges, inclinometers and displacement transducers set-up for substructures (dimensions in mm).

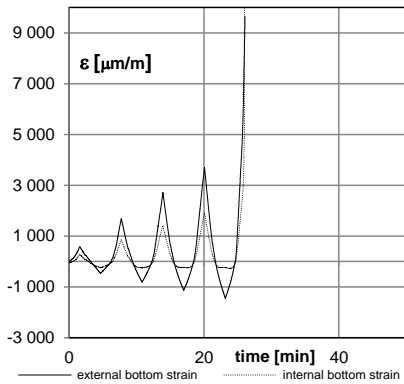


Figure 20 SSC4 test: bottom side unbonded internal vs unbonded external fibre data.

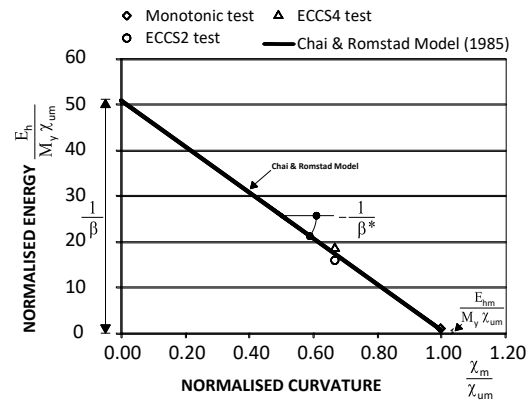


Figure 21 Damage limit domain of concrete section with parameter β^* estimation.

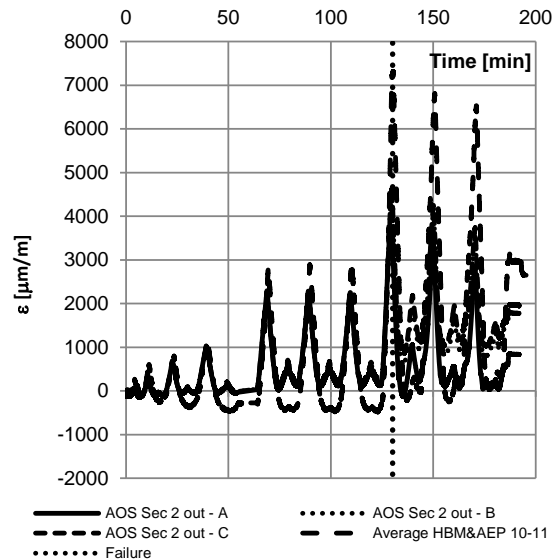
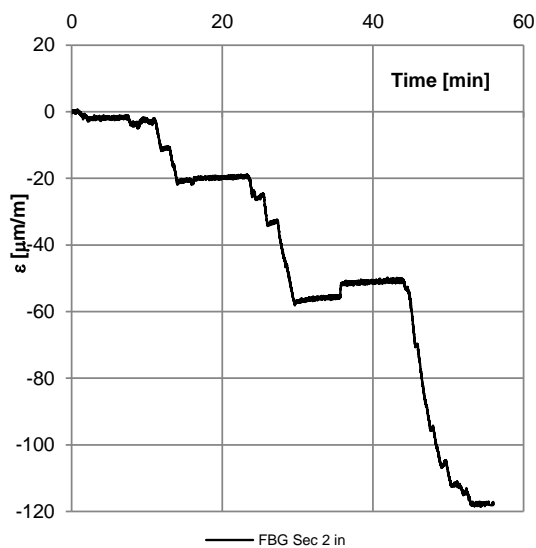


Figure 22 Test on Tunnel Lining (TLC1): a) strains owing to the prestressing of the ring section, Sec 2 In; b) comparison between Inner bonded FBG fibre data in Section 2 and standard displacements sensors, Out, during the cyclic test

Table 4
Average values of prestraining

Section	1	2	3	4	5	6	7	8
Average Out/In at the Maximum Load ($\mu\text{m/m}$)	-122	-119	-96	-42	-139	-52	-120	-115

Table 5
Maximum deformations at each instrumented section

Section	1	2	3	4	5	6	7	8
ϵ_{max} measured by fibres inside ring [%]	0.12	1.2	0.02	0.87	0.05	0.54	0.18	0.63
ϵ_{max} measured by fibres inside ring [%]	0.05	0.46	0.01	0.59	0.02	0.21	0.03	0.50

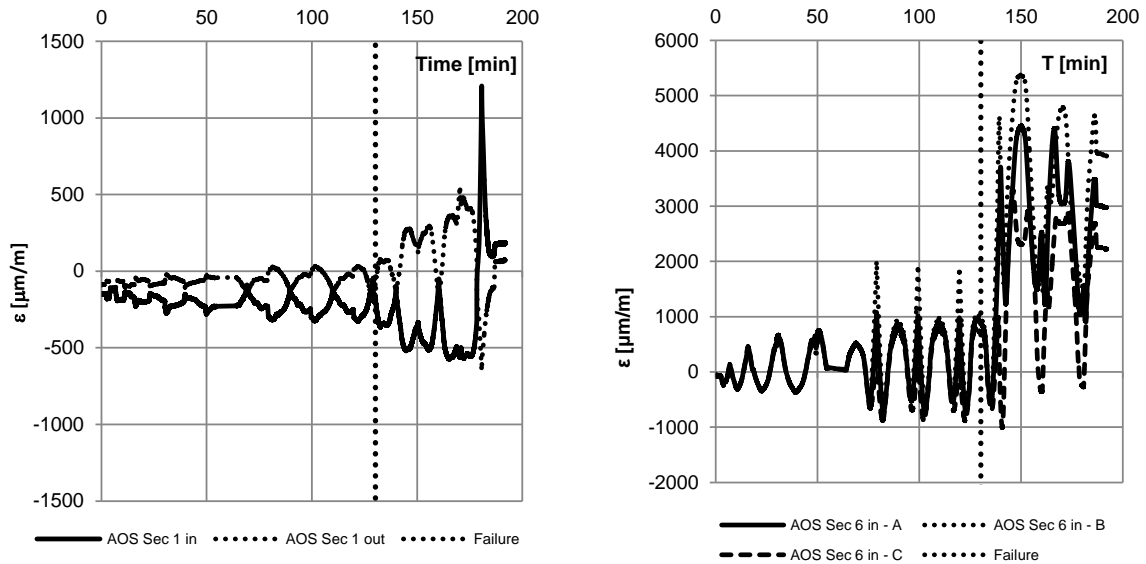


Figure 23 TLC1 test, during the ECCS phase: a) external unbonded FBG fibre data in Section 1; b) Inner unbonded FBG fibre data in Section 6, In.

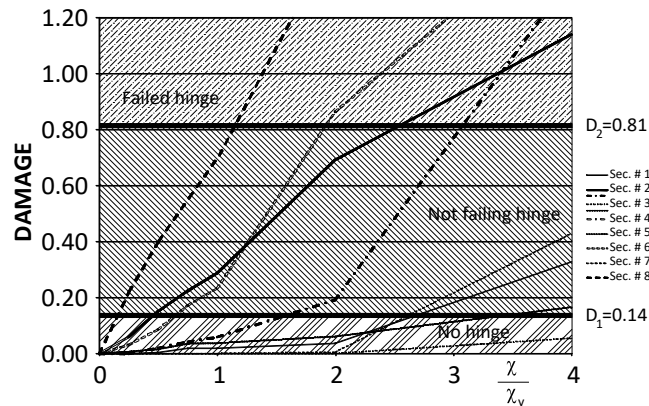


Figure 24 TLC1 test: section Damage evolution, during the ECCS phase.

ACKNOWLEDGMENTS

This work was carried out with a financial grant from the European Union Framework Programme 7 “Fibre optics-based intelligent monitoring and assessment system for proactive maintenance and seismic disaster prevention in reinforced concrete tunnel linings” (MONICO) FP7-SME-2007-1. The support of AOS for the FBG acquisition during testing is gratefully acknowledged.

REFERENCES

Adewuyi, A.P. & Wu, Z. (2011), Vibration-based damage localization in flexural structures using normalized modal macrostrain techniques from limited measurements, *Computer-Aided Civil and Infrastructure Engineering*, **26**(3), 154-172.

Bairaktaris, D., Frondistou-Yannas S., Kalles, D., Stathaki, A., Kallidromitis, V., Kotrotsios, G., Negro P. & Colombo, A. (1998), “Intelligent Monitoring of Seismic Damage in Reinforced Concrete Tunnel Linings”, Workshop on Reducing Earthquake Risks to Structures and Monuments in the EU, Cambridge, UK, 26-27.

Bursi, O.S. & Ferrario, F. (2003), Computational Models for the Low-cycle Fatigue Behaviour of Composite Members and Joints, in *Progress in Civil and Structural Engineering Computing*, Edited by B.H.V. Topping, Saxe-Coburg Publications, Stirling, 119-148.

CEN (2005), *Eurocode 2 Design of concrete structures. General rules and rules for buildings. EN 1992-1*, European Committee for Standardization, Brussels, Belgium.

Chai, Y.H., Romstad, K.M. & Bird, S. (1995), Energy Based Linear Damage Model for High-Intensity Seismic Loading. *Journal of Structural Engineering, ASCE*, **121**(5), pp. 857-864.

Cruz, P.J.S. & Salgado, R. (2009), Performance of vibration based damage detection methods in bridges, *Computer-Aided Civil and Infrastructure Engineering*, **24**(1), 62-79.

Cusson, D., Lounis, Z. & Daigle, L. (2011), Monitoring Life Cycle Performance of Aging Concrete Highway Bridges Built in Corrosive Environments, *Computer-Aided Civil and Infrastructure Engineering*, **26**(7), 524-541.

Ditlevsen, O. & Madsen, H.O. (1996), *Structural Reliability Methods*, Wiley.

Glisic, B., Chen, J. & Hubbell, D. (2011), Streicker Bridge: A comparison between Bragg-grating long-gauge strain and temperature sensors and Brillouin scattering-based distributed strain and temperature sensors, *Proceedings of SPIE - The International Society for Optical Engineering 7981*, art. no. 79812C.

Glisic, B. & Yao Y. (2012), Fiber optic method for health assessment of pipelines subjected to earthquake-induced ground movement, *Structural Health Monitoring*, **11**(6) 696-711.

Guemes, A., Fernandez-Lopez, A. & Soller, B. (2010), Optical Fiber Distributed Sensing – Physical Principles and Applications, *Structural Health Monitoring*, **9**:3, 233-245.

Habel, W.R. & Krebber, K. (2011), Fiber-Optic sensor applications in civil and geotechnical engineering. *Photonic Sensors*, **1**(3), 268-280.

Hammersley, J.M. & Handscomb, D.C. (1975), *Monte Carlo Methods*. Norwich, England, Fletcher.

Hampshire, T.A. & Adeli, H. (2000), Monitoring the Behavior of Steel Structures Using Distributed Optical Fiber Sensors, *Journal of Constructional Steel Research*, Vol. 53, No. 3, pp. 267-281.

Hashash, Y.M.A., Hook, J.J., Schmidt, B. & Yao, J.I.-C. (2001), Seismic design and analysis of underground structures, *Tunnelling and Underground Space Technology*, **16**, 247-293.

Hashash, Y.M.A., Park, D. & Chiang Yao, J. I. (2005), Ovaling deformations of circular tunnels under seismic loading, an update on seismic design and analysis of underground structures, *Tunnelling and Underground Space Technology*, **20**(5), 435-441.

Her, S-C & Huang, C-Y (2011), Effect of Coating on the Strain Transfer of Optical Fiber Sensors, *Sensors*, **11**, 6926-6941.

Huang, Y., Beck, J.L., S. Wu, S., and Li, H. (2014), Robust Bayesian compressive sensing for signals in structural health monitoring, *Computer-Aided Civil and Infrastructure Engineering*, **29**(3), 160-179.

Iman, R. L. and Conover, W. J. (1980), Small sample sensitivity analysis technique for computer models, with an application to risk assessment, *Communications in Statistics A9*-(17), pp. 1749-1874.

Khelifa, M.R. and Guessasma, S. (2013), New computational model based on finite element method to quantify damage evolution due to external sulfate attack on

self-compacting concretes, *Computer-Aided Civil and Infrastructure Engineering*, **28**(4), 260-272.

Kerrouche, A., Boyle, W.J.O., Sun, T., Grattan, K.T.V., Schmidt, J.W. & Taljsten, B. (2009), Strain Measurement Using Embedded Fibre Bragg Grating Sensors Inside an Anchored Carbon Fiber Polymer Reinforcement Pre-stressing Rod for Structural Monitoring, *IEEE Sensors Journal*, **9**(11), 1456-1461.

Kirzhner, F. & Rosenhouse, G. (2000), Numerical analysis of tunnel dynamic response to earth motions. *Tunneling and Underground Space Technology*, **15**(3), 249-258.

Loupos, K., Kanellos, G., Bursi, O.S., Frondistou, S., Meissner, J., Bairaktaris, D., Griffoni, B. & Orfanoudakis, A. (2011), Application of Fibre-Optic technologies for Real-time Structural Monitoring - The MONICO EC Project, *Proceeding of the 9th International Conference on Damage Assessment of Structures (DAMAS 2011)*, Oxford, UK, 11-13 July.

Majumder, M., Gangopadhyay, T.K., Chakraborty, A.K., Dasgupta, K., & Bhattacharya, D.K. (2008), Fibre Bragg gratings in Structural Health Monitoring - Present status and applications. *Sensors and Actuators*, **147**, 150-164.

Ministero delle Infrastrutture (2008). *Norme Tecniche per le Costruzioni* (in Italian)

Newmark, N. M. (1968), Problems in Wave Propagation in Soil and Rock, *International Symposium on Wave Propagation and Dynamic Properties of Earth Materials*

Nigro, M.B., Pakzad, S.N., and Dorvash, S. (2014), Localized Structural Damage Detection: A Change Point Analysis, *Computer-Aided Civil and Infrastructure Engineering*, **29**(6), 416-432.

Nilson, A.H. & Winter, G. (1986), *Design of Concrete Structures* 10 th Ed. McGraw, Hill, New York etc.

Park, Y.J. & Ang, A.H.-S. (1985), Mechanistic seismic damage model for reinforced concrete, *Journal of Structural Engineering*, ASCE, **111**(ST4), 722-739.

Penzien, J. & Wu, C.L. (1998), Stresses in linings of bored tunnels, *Earthquake Engineering and Structural Dynamics*, **27**, 283-300.

Penzien, J. (2000), Seismically induced racking of tunnel linings, *Earthquake Engineering and Structural Dynamics*, **29**, 683-691.

Ordinanza del Presidente del Consiglio dei Ministri N. 3274 e s.m. (3431 3 maggio 2005). *Primi elementi in materia di criteri generali per la classificazione sismica del territorio nazionale e di normative tecniche per le costruzioni in zona sismica*, 20 marzo 2003 (in Italian).

Raich, A.M. and Liskai, T.R. (2012), "Multi-Objective Optimization of Sensor and Excitation Layouts for Frequency Response Function-based Structural Damage Identification," *Computer-Aided Civil and Infrastructure Engineering*, **27**:2, pp. 95-117.

Rao, Y. J. (1997), In-fibre Bragg grating sensors, *Measurement Science and Technology*, vol. 8, no. 4, pp. 355–375.

Rodrigues, C., Félix, C., Lage, A. & Figueiras, J. (2011), Development of a long-term monitoring based on FBG sensors applied to concrete bridges. *Engineering Structures*, **3**, 1993-2002.

Szechy, K. (1970), *The art of tunnelling*, Akademiai Kiadó, Budapest.

Technical Committee 1, TWG 1.3 (1986), Recommended testing procedures for assessing the behaviour of structural steel elements under cyclic loads ECCS, No. 45.

Wang, J. N. (1993), *Seismic Design of Tunnels A Simple State-of-the-Art Design Approach*, William Barclay Parsons Fellowship, Parsons Brinckerhoff Monograph 7.

Williams, M.S. & Sexsmith, R. G. (1995), Seismic Damage Indices for Concrete Structures: A State-of-the-Art Review. *Earthquake Spectra*, **11** (2), 319-349.

Wu, Z. & Adewuyi, A.D. (2011), Identification of damage in reinforced concrete columns under progressive seismic excitation stages. *Journal of Earthquake and Tsunami*, **5**(2), 151-165.

Zhang, W., Junqi, G., Bin, S. & Heliang C. (2006), Health Monitoring of Rehabilitated Concrete Bridges Using Distributed Optical Fiber Sensing. *Computer-Aided Civil and Infrastructure Engineering*, **21**(6):411–424